



Cite as

Nano-Micro Lett.
(2024) 16:191Received: 22 January 2024
Accepted: 20 March 2024
© The Author(s) 2024

TiO₂ Electron Transport Layer with p–n Homojunctions for Efficient and Stable Perovskite Solar Cells

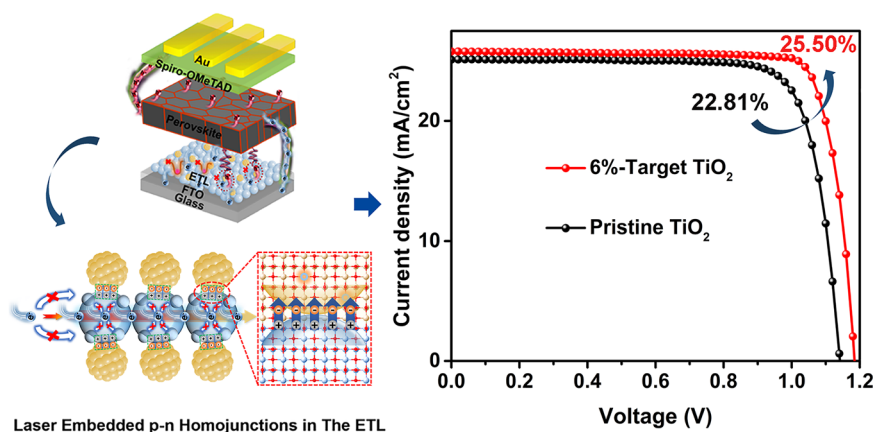
Wenhao Zhao¹, Pengfei Guo^{1,4} ✉, Jiahao Wu¹, Deyou Lin¹, Ning Jia¹, Zhiyu Fang¹,
Chong Liu¹, Qian Ye¹, Jijun Zou³, Yuanyuan Zhou², Hongqiang Wang^{1,4} ✉

HIGHLIGHTS

- Developing a universal strategy of the p–n homojunction engineering that could significantly boost electron mobility of electron transport layer (ETL) by two orders of magnitude.
- Proposing a new mechanism based on p–n homojunction to explain inhibited carrier loss at buried interface.
- Setting a new performance benchmark as high as 25.50% for planar perovskite solar cells employing TiO₂ as ETLs.

ABSTRACT Low-temperature processed electron transport layer (ETL) of TiO₂ that is widely used in planar perovskite solar cells (PSCs) has inherent low carrier mobility, resulting in insufficient photogenerated electron transport and thus recombination loss at buried interface. Herein, we demonstrate an effective strategy of laser embedding of p–n homojunctions in the TiO₂ ETL to accelerate electron transport in PSCs, through localized build-in electric fields that enables boosted electron mobility by two orders of magnitude.

Such embedding is found significantly helpful for not only the enhanced crystallization quality of TiO₂ ETL, but the fabrication of perovskite films with larger-grain and the less-trap-states. The embedded p–n homojunction enables also the modulation of interfacial energy level between perovskite layers and ETLs, favoring for the reduced voltage deficit of PSCs. Benefiting from these merits, the formamidinium lead iodide (FAPbI₃) PSCs employing such ETLs deliver a champion efficiency of 25.50%, along with much-improved device stability under harsh conditions, i.e., maintain over 95% of their initial efficiency after operation at maximum power point under continuous heat and illumination for 500 h, as well as mixed-cation PSCs with a champion efficiency of 22.02% and over 3000 h of ambient storage under humidity stability of 40%. Present study offers new possibilities of regulating charge transport layers via p–n homojunction embedding for high performance optoelectronics.

✉ Pengfei Guo, guopengfei@nwpu.edu.cn; Hongqiang Wang, hongqiang.wang@nwpu.edu.cn¹ State Key Laboratory of Solidification Processing, Center for Nano Energy Materials, School of Materials Science and Engineering, Northwestern Polytechnical University and Shaanxi Joint Laboratory of Graphene (NPU), Xi'an 710072, People's Republic of China² Department of Chemical and Biological Engineering, Hong Kong University of Science and Technology, Clear Water Bay, Hong Kong SAR, People's Republic of China³ Key Laboratory for Green Chemical Technology of the Ministry of Education, School of Chemical Engineering and Technology, Tianjin University, Tianjin 300072, People's Republic of China⁴ Chongqing Innovation Center of Northwestern, Polytechnical University, Northwestern Polytechnical University, Chongqing 401135, People's Republic of China

KEYWORDS Electron transport layer; p–n homojunction; Electron mobility; Buried interface; Perovskite solar cells

1 Introduction

Planar metal halide perovskite solar cells (PSCs) have been pushing the record-breaking power conversion efficiencies (PCEs) over 26%, as well as durable stability and compatibility with large-scale manufacture [1–3]. The reasons behind such significant achievements are associated with the strategies of integrating low-bandgap and less-trap-state formamidine-based perovskite with widely regarded as efficient charge transport layers [4]. In particular, regular planar PSCs indispensably necessitate high-quality and compatible electron transport layer (ETL) owing to their high light transmittance, suitable energy level, and low-temperature processability, which are crucial to not only the growth of the top perovskite grain but also extraction and collection of the photogenerated electrons to the electrode [5]. While noting that widely adopted metal oxide ETLs are inevitably endowed with inherently inferior electron mobility (for example, TiO_2 : usually at the level of $10^{-5} \sim 10^{-4} \text{ cm}^2 \text{ V}^{-1} \text{ s}^{-1}$) due to low-temperature process that could arouse charge carrier accumulation and recombination loss at buried interface, resulting in less-than-ideal efficiency and unrobust environmental stability [6]. Several state-of-the-art engineering strategies have been developed to address the imperfections of such ETLs, as exemplified by employing nitrogen-doped TiO_2 ETLs with reduced the electrical series resistance, as well as high-lattice-matching SrSnO_3 as the ETLs enabling ordered beginning of the growth of perovskite to synchronously rule the buried defects and carrier dynamics in PSCs [7, 8].

Creation of p–n junction either in the active layer or at upper/buried interface has been exploited as an effective strategy to tune the charge carrier transport in PSCs [9, 10]. For example, embedding 2D graphdiyne or 0D fluorinated-gold-cluster at grain boundaries within the perovskite films enables the construction of p–n heterojunctions, which provides an extra channel to favor the exciton separation and charge transport [11, 12]. It is reported that the TiO_2 with Ti vacancies shows inherent p-type conductivity with high charge mobility, demonstrating a nearly sevenfold increase over the normal n-type TiO_2 [13]. Motivated by embedding

p–n junction in perovskite to alleviate the carrier loss, it would thus be highly promising to construct the p–n homojunction in the ETLs by introducing Ti-defected TiO_2 in n-type TiO_2 for further pronounced electron conducting capability and highly efficient and stable TiO_2 -based planar PSCs. The challenge however remains on not only the technical embedding of such p-type TiO_2 in n-type TiO_2 ETLs, but also the understanding of such homojunction influencing the carriers transport in the ETL.

Present work demonstrates an effective strategy of constructing $\text{Ti}_{0.936}\text{O}_2@ \text{TiO}_2$ -based p–n homojunction to improve electron mobility and photovoltaic performance of planar PSCs through embedding laser-derived p-type $\text{Ti}_{0.936}\text{O}_2$ in TiO_2 ETL. Such embedding of Ti-defected TiO_2 could modulate the crystallization kinetics of the TiO_2 matrix by restraining the rutile phase that is detrimental to light stability of PSCs, contributing to the formation of high-quality TiO_2 ETLs. The formed p–n homojunction enables also not only elimination of the interfacial lattice distortion between $\text{Ti}_{0.936}\text{O}_2$ and TiO_2 , but also more efficient transport of charge carriers at both surfaces and boundaries of TiO_2 ETLs through localized build-in electric fields, thus reducing the recombination loss (Scheme 1). More importantly, such a novel $\text{Ti}_{0.936}\text{O}_2@ \text{TiO}_2$ composite ETL has also exerted a significant influence on the construction of less-trap-states and larger-grain perovskite films. Benefiting from these merits, we obtain highly efficient formamidinium lead iodide (FAPbI₃) PSCs with PCE up to 25.50%, which ranks as far as we know among the top in records of TiO_2 -based planar PSCs. Owing to the synchronous regulation of the $\text{Ti}_{0.936}\text{O}_2$ in photocatalytic activity of TiO_2 ETLs and film quality of perovskite layers, we have also obtained highly stable FAPbI₃ PSC that maintains over 95% of their initial efficiency at maximum power point under continuous illumination for 500 h, as well as mixed-cation PSCs with pronounced environmental stability over 3000 h under RH of 40%. We believe this study provides an efficient alternative of improving the carrier conducting capability for charge transport layers and their optoelectronic devices, from the viewpoint of p–n homojunction engineering.

For the preparation of target ETL: an approximately 50 nm thick TiO₂ compact layer deposited on clean FTO substrate is prepared adopting in situ chemical bath co-deposition by adding different volume of Ti_{0.936}O₂ colloid solutions (3%, 6%, and 9% volume ratio to TiCl₄ precursor abbreviated as 3%-Target TiO₂, 6%-Target TiO₂, 9%-Target TiO₂) to TiCl₄ aqueous solution (2.25: 100 volume ratio of TiCl₄: H₂O), along with FTO substrates suffering from thermal treatment at 70 °C for 1 h, and then anneal at 150 °C for 1 h.

For the preparation of pristine ETL: identical TiCl₄ aqueous solution without adding Ti_{0.936}O₂ colloid solutions, along with FTO substrates are subjected to similar thermal processing mentioned above.

2.2.3 Fabrication of Perovskite Solar Cells

CsFAMA type perovskite: CsI (0.0625 M), FAI (1.0125 M), PbI₂ (1.075 M), MABr (0.175 M) and PbBr₂ (0.175 M) is dissolved in a mixture of DMF: DMSO (4:1 v/v) with a successive stir at 55 °C for 2 h to prepare precursor solution at a concentration of 1.25 M. The spin-coating process was performed in a nitrogen glove box. The as-prepared precursor (30 μL) was dropped onto the TiO₂/FTO substrate followed by a consecutive two-step spin-coating process at 2000 and 4000 rpm for 10 and 30 s, respectively. During the second spin-coating step, 200 μL anhydrous chlorobenzene (CB) was immediately poured on the substrate 10 s prior to the end of the program. Subsequently, the intermediate phase film is heated on a hotplate at 100 °C for 1 h.

FAPbI₃ type perovskite: FAI (1.80 M), PbI₂ (1.80 M), FAHCOO (0.12 M), and MACl (0.52 M) are dissolved in a mixture of DMF: DMSO (volume ratio = 4:1) at 55 °C for 2 h to prepare the perovskite precursor (1.80 M). The as-prepared precursor (30 μL) was dropped onto the TiO₂/FTO substrate followed by a one-step spin-coating at 6500 rpm for 60 s. During spin coating, 200 μL chlorobenzene (CB) is immediately poured on the substrate 20 s prior to the end of the program. Subsequently, the intermediate phase film is heated on a hotplate at 150 °C for 10 min.

In addition, for FAPbI₃ type perovskite, 3 mg ml⁻¹ phenethylammonium iodide (PEAI) was deposited on the perovskite/TiO₂/FTO substrate via a one-step spin-coating

process at 4000 rpm for 30 s, followed by deposition of Spiro-OMeTAD.

Spiro-OMeTAD solution was prepared by dissolving 72.3 mg Spiro-OMeTAD, 29 μL 4-*tert*-butylpyridine (tBP) and 18 μL lithium-bis (trifluoromethanesulfonyl) imide (Li-TFSI, a stock solution of 520 mg mL⁻¹ in acetonitrile) into 1 mL chlorobenzene. And then 30 μL solution was spin-coated on the perovskite/TiO₂/FTO substrate at 6000 rpm for 30 s. Finally, the Au electrode (80 nm) was deposited on the top of devices by thermal evaporation using a shadow mask. Each electrode of devices exhibits the area of 0.05 cm², for which the effective area would be corrected by optical microscopy.

2.3 Characterization

The scanning electron microscopy (SEM) images were obtained using a field emission SEM (FEI Nova). Atomic force microscope (AFM) was carried out using a Bruker Dimension Icon. High-resolution transmission electron microscopy (HRTEM) was conducted employing an FEI Tecnai F30 transmission electron microscope at 300 kV, equipped with an Oxford Instruments EDS detector and a high angle annular dark field (HAADF) STEM detector. The Raman spectra were recorded by a Raman microscope at an excitation laser wavelength of 532 nm (Renishaw). The X-ray diffraction (XRD) patterns were recorded on a X'pert PRO (PANalytical) adopting a Cu Kα (λ = 0.15406 nm) as the X-ray source. The absorption was characterized by the ultraviolet–visible (UV–vis) spectrophotometer (Perkin-Elmer Lambda 35 UV–vis-NIR). The steady-state photoluminescence (PL) and time-resolved photoluminescence (TRPL) spectra were recorded by a pulse laser excitation source at the wavelength of 470 nm (Horiba FluorologFL-3). The electrical impedance spectroscopy (EIS) was characterized applying a bias of 0.8 V in the dark in a frequency range from 1 MHz to 0.1 Hz (CHI660E). For Mott-Schottky analysis, capacitance–voltage measurements were performed at a frequency of 1 kHz (CHI660E). X-ray photoelectron spectroscopy (XPS) measurements were conducted on an Axis Supra (Kratos). Ultraviolet photoelectron spectroscopy (UPS) was characterized by a VG Scienta R4000 analyzer and the HeI (21.22 eV) emission line employed for excitation at a bias of –5 V. The contact angles measurements were

conducted by a data physics OCA-20 contact-angle system at ambient air. Temperature dependent admittance spectroscopy (TAS) was performed on a precision impedance analyzer at various temperatures ($T = 210\text{--}320\text{ K}$) in the dark. A Keithley 2400 source meter was used to record the $J\text{--}V$ curves and maximum power point tracking under simulated AM 1.5G illumination (100 mW cm^{-2}) produced by a xenon-lamp-based solar simulator (Oriel 67005, 150 W Solar Simulator), which was calibrated with a monocrystalline silicon reference cell (Hamamatsu S1133). The devices were measured both in reverse scan ($+1.2\text{--}0.1\text{ V}$) and forward scan ($-0.1\text{--}+1.2\text{ V}$) with a scanning rate of 0.2 V s^{-1} . The EQE was conducted by employing a Enlitech EQE measurement system (QE-R3011). A Keithley 2400 source was used to measure the dark $I\text{--}V$ characterization of the electron-only devices for calculating the defect density using SCLC model.

2.4 Statistical Analysis

All quantitative values are shown as means \pm standard deviation. All quantitative experiments were carried out using at least three replicates for each group. The statistical analysis was conducted by the t test, and a p value of less than 0.05 was considered as statistical significance. The error bars correspond to the standard deviation of data points from individual samples.

3 Results and Discussion

3.1 Laser Embedding of p-Type $\text{Ti}_{0.936}\text{O}_2$ Nanocrystals in TiO_2 ETLs

Laser manufacture of size-tailored $\text{Ti}_{0.936}\text{O}_2$ nanocrystals by irradiation of their raw sub-micrometer counterpart in liquid and subsequent embedding in the TiO_2 matrix through the chemical bath deposition method are shown in Figs. S1 and S2. Subsequent to the optimization of laser fluence and concentration of laser process (Fig. S3), the transparent $\text{Ti}_{0.936}\text{O}_2$ colloid solution with clear Tyndall scattering is obtained with well-dispersed nanocrystals with an average diameter of 3.5 nm (Fig. 1a). The crystal structure of the as-prepared $\text{Ti}_{0.936}\text{O}_2$ nanocrystals, which was determined by HRTEM and corresponding Fast Fourier transform (FFT), represents the lattice spacing of 0.24 nm that corresponds

to the typical plane (004) of $\text{Ti}_{0.936}\text{O}_2$ (Fig. 1b), further confirmed by their identical Raman spectroscopy (Fig. S4). These results indicate that $\text{Ti}_{0.936}\text{O}_2$ nanocrystals well inherit the properties of their bulk counterpart. In addition, the elements mapping extracted from TEM-energy-dispersive spectroscopy (TEM-EDS) suggests homogeneous distribution of all elements throughout the entire $\text{Ti}_{0.936}\text{O}_2$ nanoparticles without any segregation (Fig. S5). Furthermore, the XPS demonstrate stable surface composition and chemical state of the $\text{Ti}_{0.936}\text{O}_2$ during laser irradiation (Fig. S6) [13]. This is consistent with the recent work that reflects unchanged Ti-vacancy of laser-processed $\text{Ti}_{0.936}\text{O}_2$ characterized by electron paramagnetic resonance (EPR) spectroscopy [14].

Subsequently, the deposition of $\text{Ti}_{0.936}\text{O}_2@\text{TiO}_2$ ETL was conducted adopting a facile one-step chemical bath co-deposition, where laser-generated sub-5 nm $\text{Ti}_{0.936}\text{O}_2$ nanocrystals could be in situ embedded in the TiO_2 matrix (Fig. S7). In brief, different contents (3%, 6%, and 9% volume ratio to TiCl_4 precursor denoted as 3%-target TiO_2 , 6%-target TiO_2 , 9%-target TiO_2) of $\text{Ti}_{0.936}\text{O}_2$ colloids with concentration of 0.1 mg mL^{-1} were incorporated into TiCl_4 solution to fabricate the TiO_2 composite ETLs. Scanning electron microscopy (SEM) and atomic force microscopy (AFM) were performed to evaluate the surface morphologies of corresponding TiO_2 films. The results reveal that the 6%-target TiO_2 film exhibits smoother and flatter surface with reduced roughness from 33.8 to 21.5 nm in comparison with the pristine film, as shown in Figs. 1c and S8. In order to further explore the influence of embedding $\text{Ti}_{0.936}\text{O}_2$ on crystallization kinetics of TiO_2 ETLs, the settled TiO_2 powders after chemical bath co-deposition were collected for systematic XRD analysis. As shown in Fig. 1d, the initial TiO_2 ETL consists of polymorphic phases of rutile and anatase, while the rutile phase in the ETLs is significantly reduced after the embedding of $\text{Ti}_{0.936}\text{O}_2$. It should be noted that the fast nucleation rate is more inclined to form the anatase phase at the initial stage of TiCl_4 hydrolysis, whereas the slow nucleation rate is conducive to the directional arrangement of aggregates, resulting in the generation of a more stable rutile phase [15]. It could thus be deduced that the addition of $\text{Ti}_{0.936}\text{O}_2$ favors the rapid nucleation, which enables not only the formation of smaller TiO_2 grains for their compact deposition, but the inhibition of rutile phase and anatase–rutile hetero-phase junction for reducing the unwanted photocatalytic degradation of PSCs under continuous light soaking [16, 17].

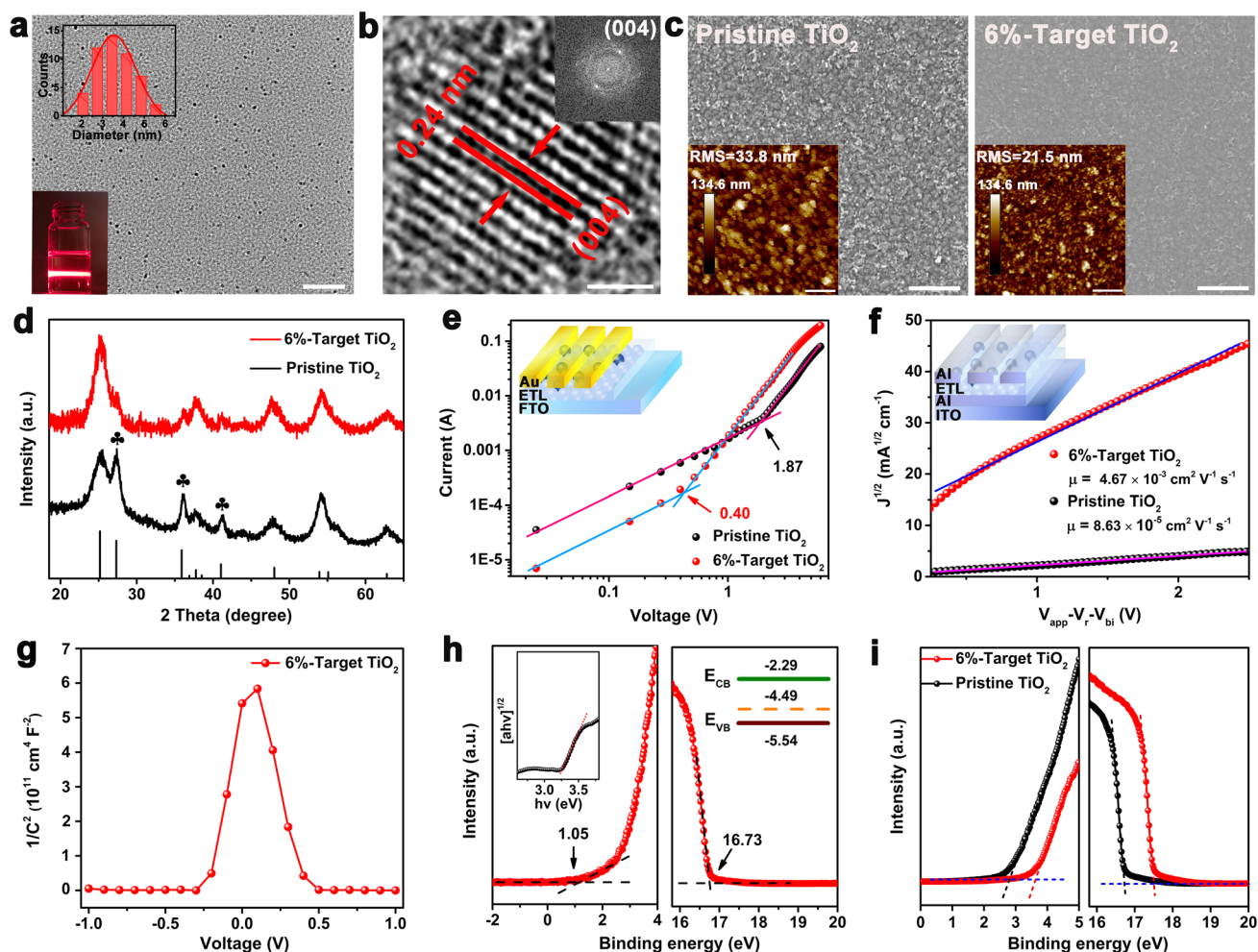


Fig. 1 **a** TEM image of $\text{Ti}_{0.936}\text{O}_2$ nanocrystals (inset: nanocrystals size distribution diagram and Mie-scattering image of colloids). **b** HRTEM and corresponding FFT of $\text{Ti}_{0.936}\text{O}_2$ nanocrystals. **c** SEM images (inset: AFM images) of pristine TiO_2 and 6%-target TiO_2 films. **d** XRD patterns of different ETLs. **e** Dark I - V measurement of the electron-only devices (inset) displaying V_{TFL} kink point related to the trap density. **f** Electron mobilities of different ETLs using the SCLC model, the inset shows the device structure of ITO/Al/ETLs/Al. **g** Mott-Schottky plots of $\text{Ti}_{0.936}\text{O}_2$ @ TiO_2 matrix. **h** UPS results of $\text{Ti}_{0.936}\text{O}_2$ nanocrystals (inset: band gap and energy level of $\text{Ti}_{0.936}\text{O}_2$ nanocrystals). **i** Different TiO_2 films with UPS Fermi edge (left) and the cut-off energy (right). Scale bar: **a** 50 nm; **b** 1 nm; **c** 1 μm (inset: 1 μm)

In order to investigate the effects of the $\text{Ti}_{0.936}\text{O}_2$ nanocrystals on the optical and electronic properties of the TiO_2 ETLs, the optical bandgap of $\text{Ti}_{0.936}\text{O}_2$ @ TiO_2 films were first evaluated by ultraviolet–visible (UV–vis) absorption spectra and corresponding Tauc plots. The results show that the embedding of $\text{Ti}_{0.936}\text{O}_2$ enables slight increase in the bandgap of the TiO_2 ETLs from 3.20 to 3.22 eV, with insignificant change on the optical transmittance, as shown in Figs. S9 and S10. To evaluate the electronic properties, the defect density (N_t) and the electron mobility (μ) of the TiO_2 ETLs were successively examined by the space charge-limited current (SCLC) method. The result shows that the

embedding of $\text{Ti}_{0.936}\text{O}_2$ results in the reduction of N_t from initial 6.48×10^{16} – $1.39 \times 10^{16} \text{ cm}^{-3}$ (Fig. 1e and Table S1), which may be due to the improved crystallization kinetics of TiO_2 and the high-quality ETLs. Moreover, the μ is found to be boosted by two orders of magnitude from pristine 8.63×10^{-5} – $4.67 \times 10^{-3} \text{ cm}^2 \text{ V}^{-1} \text{ s}^{-1}$ for the 6%-target TiO_2 ETLs (Fig. 1f), which is consistent with the conductivity (σ) result that indicates higher σ for 6%-target TiO_2 due to a large slope (Fig. S11). The improved electronic properties are mainly attributed to the construction of $\text{Ti}_{0.936}\text{O}_2$ @ TiO_2 p–n homojunction, which is evidenced by an inverted “V-shape” with typical p–n junction feature from the Mott-Schottky plot

shown in Fig. 1g [18]. To confirm the p-type characteristic of the $\text{Ti}_{0.936}\text{O}_2$, the ultraviolet photoelectron spectroscopy (UPS, Fig. 1h) was used to check its electronic structure of the $\text{Ti}_{0.936}\text{O}_2$. Based on the optical bandgap (3.25 eV) (inset in Fig. 1h), the corresponding Fermi energy level, the conduction band energy level and the valence band energy level are calculated to be -4.49 , -2.29 , and -5.54 eV, respectively, which identifies the p-type semiconductor feature of the $\text{Ti}_{0.936}\text{O}_2$ nanocrystals. Such p–n construction greatly accelerates the carrier transport at both the surfaces and the boundaries of TiO_2 particles to restrain carrier loss owing to the increase of the depletion width [18, 19]. It is also found that the embedded p–n homojunction is helpful to improve electronic structure of TiO_2 ETLs with upward-shifted energy level, enabling a better energy level alignment with top perovskite active layer to lower the interfacial electron barrier (Figs. 1i and S12) [9]. Detailly, the UPS characterization of laser-processed $\text{Ti}_{0.936}\text{O}_2$ nanocrystals strongly confirms their p-type semiconductor characteristic (Fig. 1h), which were embedded into the n-type TiO_2 matrix to form a p–n junction by generating a uniform Fermi level (Fig. S12b). It is worth noting that the formed p–n homojunctions between $\text{Ti}_{0.936}\text{O}_2$ and TiO_2 could create numerous localized built-in electric fields with a direction from n-type TiO_2 to p-type $\text{Ti}_{0.936}\text{O}_2$, as shown in Scheme 1 and Fig. S12b, which enables not only the effective promotion of carrier transport at both the surfaces and boundaries of TiO_2 matrix due to the expansion of the depletion width [19], but also the oriented transport of photo-generated charge carriers, which favors for the boosted electron mobility (Scheme 1) [10].

3.2 Effect of $\text{Ti}_{0.936}\text{O}_2@ \text{TiO}_2$ on the Top Perovskite Films

The surface morphologies of the mixed-cation perovskite ($\text{Cs}_{0.05}(\text{FA}_{0.85}\text{MA}_{0.15})_{0.95}\text{PbI}_{2.55}\text{Br}_{0.45}$, CsFAMA) grown on different TiO_2 ETLs were intentionally evaluated by the SEM and AFM characterizations. The results show obviously larger-grain size and smoother surface of target perovskite films compared with those of pristine ones (Figs. 2a, b and S13). Such surface morphology can trigger the reduction of Gibbs free energy for heterogeneous nucleation of perovskite precursor due to the sharply decreased contact angle from pristine 13° – 4° , for $\text{Ti}_{0.936}\text{O}_2@ \text{TiO}_2$ ETLs (see

insets in Fig. 2a, b), thus contributing to the high-quality and large-grain perovskite films [20]. Cross-sectional SEM and XRD patterns demonstrate the large grains throughout the entire thickness of the perovskite film deposited on $\text{Ti}_{0.936}\text{O}_2@ \text{TiO}_2$ ETLs (Figs. S14 and S15), owing probably to the enhanced crystallization kinetics during their grain growth [6]. Furthermore, the steady-state and time-resolved PL spectra were employed to investigate the effects of $\text{Ti}_{0.936}\text{O}_2$ nanocrystals on the carrier dynamics between the perovskite layer and the ETLs. As shown in Fig. 2c, the CsFAMA perovskite films based on the 6%-target TiO_2 present a more prominent PL quenching with a twofold decrease of the PL intensity compared with the control films, demonstrating more efficient electron transfer between the perovskite layer and the ETLs. Similarly, time-resolved PL (TRPL) results (Fig. 2d, Table S2) exhibit that the average carrier lifetimes are calculated to be 130.63–37.38 ns for the control and the target, respectively, indicating the significant reduction of the carrier lifetime and thereby the enhanced electron extraction at the buried interface [16].

In order to further explore the impact of $\text{Ti}_{0.936}\text{O}_2@ \text{TiO}_2$ ETLs on modulating defect states in top perovskite films, temperature dependent admittance spectroscopy (TAS) was accordingly employed to quantitatively estimate both the energy level and the distribution of trap states (Note S1, Fig. S16) [21]. As shown in Fig. 2e, the defect activation energies (E_a) of different films are extracted from the Arrhenius plots of the characteristic transition frequencies obtained from the corresponding capacitance-frequency curves under different temperatures (Fig. S16a, b), and are calculated to be 0.277 and 0.223 eV for the control and target films respectively. Figure 2f exhibits the energy level and the density of trap states of different perovskite films, demonstrating that $\text{Ti}_{0.936}\text{O}_2@ \text{TiO}_2$ ETLs effectively reduce the energy level of trap states from pristine 0.22–0.18 eV, as well as their density of states from pristine 3.52×10^{16} – $2.03 \times 10^{16} \text{ cm}^{-3}$. Subsequently, the short-circuit current density (J_{sc}) and the open-circuit voltage (V_{oc}) at variable light intensities were measured to gain in-depth understanding of the carrier recombination kinetics in perovskite films. As shown in Fig. 2g, the curves of dependence of J_{sc} on the irradiation intensity represent similar slopes close to 1, revealing negligible bimolecular recombination within all films [22]. Figure 2h depicts V_{oc} versus light intensity in which the fitted slopes significantly decrease from pristine 1.50–1.05 kT/e for target films, indicating the effectively

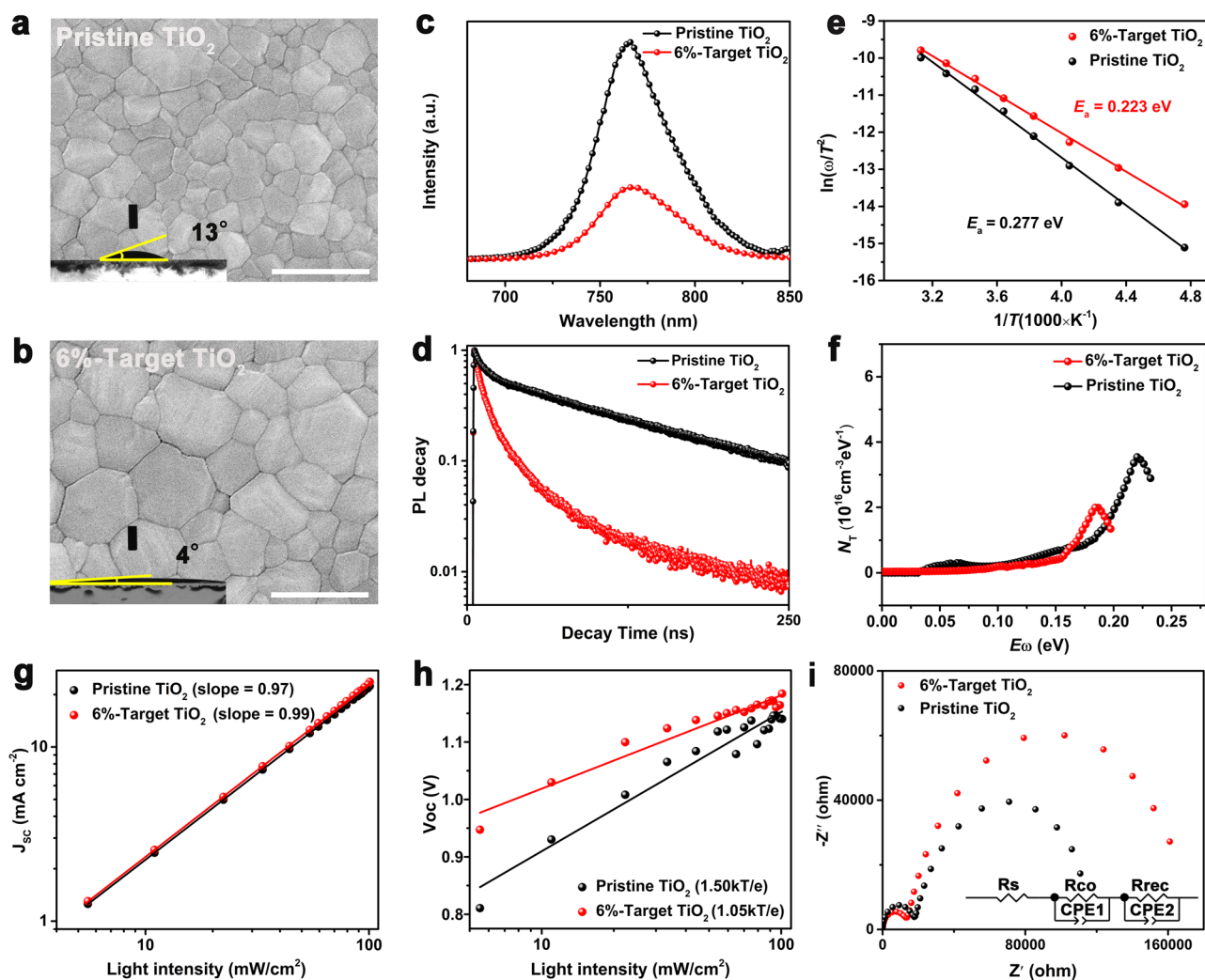


Fig. 2 SEM top-view images of perovskite films based on **a** pristine TiO_2 and **b** 6%-target TiO_2 films (inset: contact angles of different ETLs dropped by perovskite precursor). Steady-state **c** and time-resolved **d** PL spectra of CsFAMA perovskite films spin-coated on different TiO_2 layers. **e** Arrhenius plots of the characteristic transition frequencies. **f** Trap state density (N_T) of the perovskite photovoltaics measured at 300 K. Dependence of **g** J_{sc} and **h** V_{oc} on the irradiation intensity of the devices based on different TiO_2 ETLs. **i** Nyquist plots of the devices based on different ETLs measured in the dark at a bias of 0.8 V. Scale bar: **a** 500 nm; **b** 500 nm

suppressive trap-assisted recombination that facilitates leakage current (Fig. S17) [22], which is also in good agreement with that of the TAS in Fig. 2f. The EIS was used to reflect interfacial charge transfer capability between the perovskite layer and ETLs. As shown in Fig. 2i, the contact resistance (R_{co}) decreases from pristine 16,544–12,300 Ω and the recombination resistance (R_{rec}) increases from pristine 1.05×10^5 – $1.64 \times 10^5 \Omega$ for the 6%-target TiO_2 (Table S3). These results indicate that embedding of the $\text{Ti}_{0.936}\text{O}_2$ in TiO_2 matrix results in effectively improved charge transport and suppressed charge recombination at the buried interface [16, 23, 24].

3.3 Photovoltaic Performance and Stability of Planar PSCs Based on $\text{Ti}_{0.936}\text{O}_2@/\text{TiO}_2$ ETLs

The regular planar PSCs with the configuration of FTO substrate/ $\text{Ti}_{0.936}\text{O}_2@/\text{TiO}_2$ /perovskite/Spiro-OMeTAD/Au were fabricated to further evaluate the effect of the embedding of $\text{Ti}_{0.936}\text{O}_2$ on photovoltaic performance (See schematic illustration of fabrication process in Fig. S18). Figure 3a shows the current density–voltage (J – V) curves of different CsFAMA champion devices measured under illumination of 100 mW cm^{-2} (AM 1.5G) and the corresponding photovoltaic parameters are listed in Table 1. The device based

on 6%-target TiO_2 ETLs exhibits a PCE of 22.02% with a V_{oc} of 1.194 V, a J_{sc} of 23.72 mA cm^{-2} , and a fill factor (FF) of 77.75%, higher than those of devices based on pristine TiO_2 (19.94%), 3%-target TiO_2 (21.42%), and 9%-target TiO_2 (20.66%). In addition, negligible hysteresis is shown in target champion devices with a stabilized power output of 21.90% close to maximum efficiency (Fig. 3b), evidenced by reduction of hysteresis factor from pristine 13.1%–1.5% for the 6%-target TiO_2 -based devices (Table S4). To verify the universality of $\text{Ti}_{0.936}\text{O}_2@/\text{TiO}_2$ ETLs in enhancing carrier dynamics at buried interface, α -phase formamidinium lead iodide (FAPbI₃)-based devices were further constructed to pursue higher photovoltaic performance. It is worth noting that $\text{Ti}_{0.936}\text{O}_2@/\text{TiO}_2$ ETLs could encouragingly initiate the fabrication of highly crystalline FAPbI₃ perovskite with optimized morphology, and enable enhanced carrier dynamics at the buried interface (Figs. S19, S20, S21, S22, S23, Table S5). Owing to these merits, the target FAPbI₃ PSC upon a bandgap of 1.53 eV (Fig. S24) achieved the champion PCE up to 25.50% with a V_{oc} of 1.185 V, a J_{sc} of 25.79 mA cm^{-2} , and a FF of 83.45%, and highly stabilized PCE of 25.42%, far exceeding that of the control (22.81%), as shown in Fig. 3c and Table 1. Figure 3d further exhibits external quantum efficiency (EQE) spectra, in which enhanced spectral response of target devices in entire range is due to the construction of high-quality and large-grain perovskite films deposited on $\text{Ti}_{0.936}\text{O}_2@/\text{TiO}_2$ ETLs [25], enabling an increment of integrated J_{sc} from 24.27 to 25.43 mA cm^{-2} , matching well with the J - V results. As shown in Fig. 3e, efficiency distribution histogram of 50 individual PSCs indicates the improved reproducibility of the target devices, demonstrated by enhanced average PCEs from 18.28% to 21.22% and from 21.24% to 23.52% that successively corresponds to CsFAMA and FAPbI₃ PSCs, along with synchronous improvement of V_{oc} , J_{sc} and FF (Figs. S25 and S26). It is worth noting that champion efficiency of 25.50% in present work ranks among the top in records of PSCs based on TiO_2 ETLs (Fig. 3f, Table S6). Such significant enhancement in efficiency is partially attributed to the optimized interface band-alignment induced by the embedding of $\text{Ti}_{0.936}\text{O}_2$ (Fig. 3g), thereby favoring the less charge accumulation at the interface between perovskite and ETL and the increment of voltage output, evidenced by the UPS analyses and capacitance–voltage measurements (Figs. S16c and S27) [26–28].

Adopting the p–n homojunction embedding strategy has been demonstrated to be greatly effective for the construction of high-performance device, while its influence on the long-term stability of devices would be further investigated. Figure 4a shows the humidity stability of different CsFAMA PSCs without encapsulation stored in ambient air with relative humidity (RH) of 40% in the dark. The result indicates that the target devices exhibit superior humidity stability, maintaining 85% of initial PCE for 3300 h in comparison with that of control devices (approximately 50% for 700 h). The operational stability of target devices also shows great improvement, retaining 93% of initial PCE over 170 h in contrast with that of control devices (approximately 21% for 35 h), which was measured using maximum power point (MPP) tracking under full-sun illumination in ambient air with RH of $55 \pm 5\%$, as well as excellent thermal stability (Figs. 4b and S28). We further check the environmental stability of various FAPbI₃-based devices, due to the ease with which FAPbI₃ perovskite could arouse its spontaneous phase transition from α - to δ -FAPbI₃ under ambient conditions [29]. For the humidity stability of FAPbI₃ PSCs (RH of 40%, Fig. 4c), the control devices continuously degrade by more than 60% of their initial PCE for 1000 h, whereas the target devices could retain 73% of their initial value at the same time. For the operational stability of FAPbI₃-based devices under MPP tracking at 60 °C under full-sun illumination in inner atmosphere, the enhanced operational stability in target FAPbI₃ device is demonstrated by less than 5% degradation of its initial PCE over 500 h, compared with that of control devices (over 50% after 200 h, Fig. 4d). The PL characterization was further carried out to check the stability of perovskite films under continuous UV irradiation. As shown in Fig. 4e, f, there is a red shift of about 3 nm in the PL peak of pristine perovskite film under UV irradiation of 20 h, while target perovskite films on $\text{Ti}_{0.936}\text{O}_2@/\text{TiO}_2$ ETLs exhibit a negligible shift, demonstrating suppressive decomposition of perovskite film due to significantly reduced anatase–rutile phase junctions that trigger the photocatalytic property of TiO_2 [30], which accounts for improvement of light-illumination stability of target device.

It is encouragingly found that the $\text{Ti}_{0.936}\text{O}_2@/\text{TiO}_2$ ETLs play an important role in the construction of highly efficient and stable PSCs through multiple pathways: (i) the formation of the p–n homojunctions between $\text{Ti}_{0.936}\text{O}_2$ and

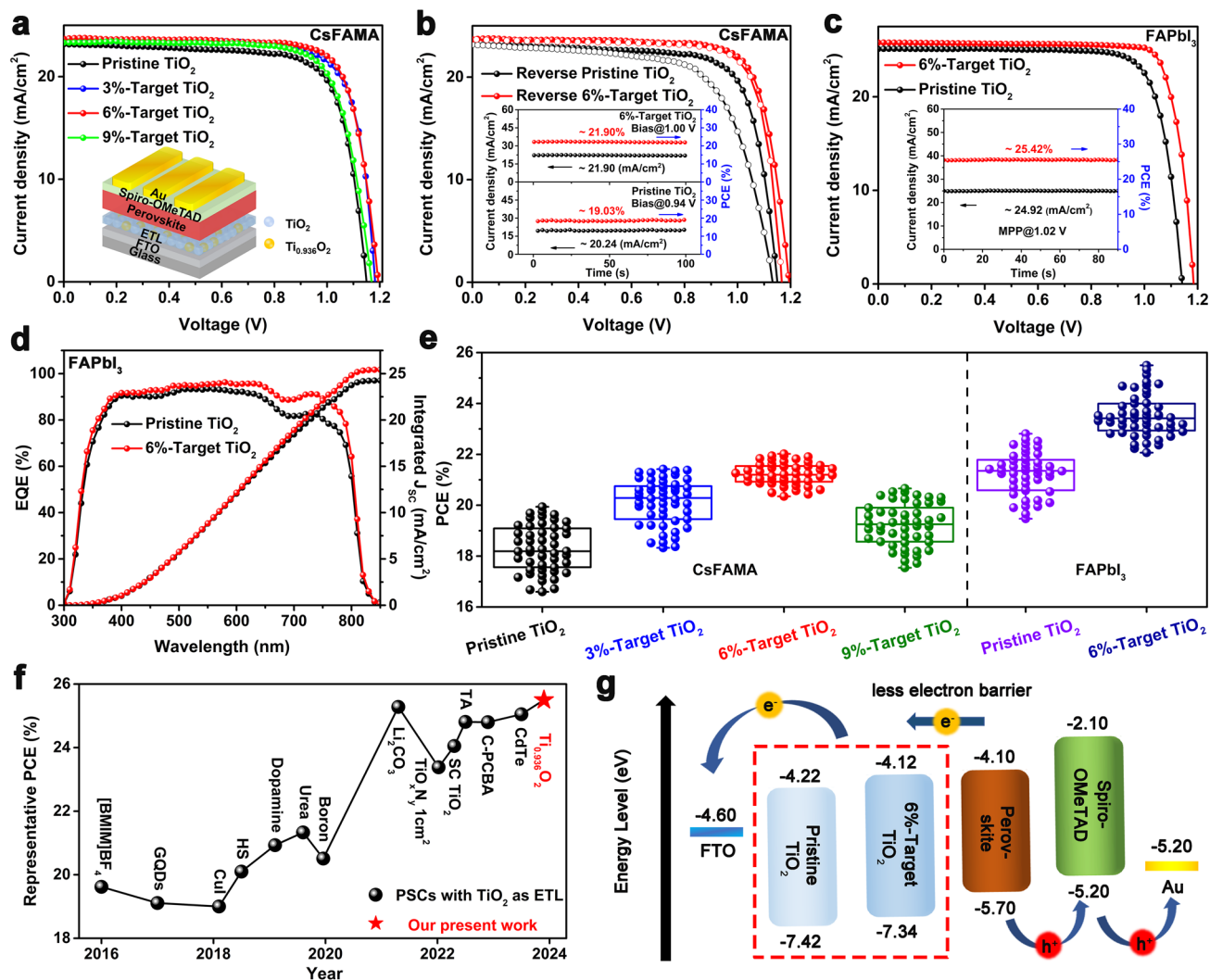


Fig. 3 **a** J - V curves of CsFAMA devices with different TiO_2 layers (inset: schematic illustration of device structure). **b** J - V plots of CsFAMA champion devices containing the pristine TiO_2 and 6%-target TiO_2 layers measured both in reverse scan and forward scan, the insets show stabilized power output at MPP tracking. **c** J - V curves of FAPbI₃ devices employing different TiO_2 layers with stabilized power output at MPP tracking. **d** EQE spectra of FAPbI₃ champion devices upon the pristine TiO_2 and 6%-target TiO_2 layers, respectively. **e** PCE distribution of 50 individual CsFAMA and FAPbI₃ devices. **f** Comparison of efficiency of PSCs employing TiO_2 as ETLs. **g** Energy level diagram for each component of devices upon different TiO_2 layers. The energy level structures of Spiro-OMeTAD and Au refer to the literature [23, 24]

Table 1 Photovoltaic parameters of the CsFAMA and FAPbI₃ type PSCs upon different TiO_2 ETLs

Sample	Content of $\text{Ti}_{0.936}\text{O}_2$ (%)	V_{OC} (V)	J_{SC} (mA cm^{-2})	FF (%)	PCE (%)	Average PCE (%)
Pristine TiO_2	0	1.149	23.16	74.93	19.94	18.28
3%-Target TiO_2	3	1.181	23.50	77.18	21.42	20.13
6%-Target TiO_2	6	1.194	23.72	77.75	22.02	21.22
9%-Target TiO_2	9	1.169	23.32	75.80	20.66	19.24
Pristine FAPbI ₃	0	1.142	25.10	79.57	22.81	21.24
Target FAPbI ₃	6	1.185	25.79	83.45	25.50	23.52

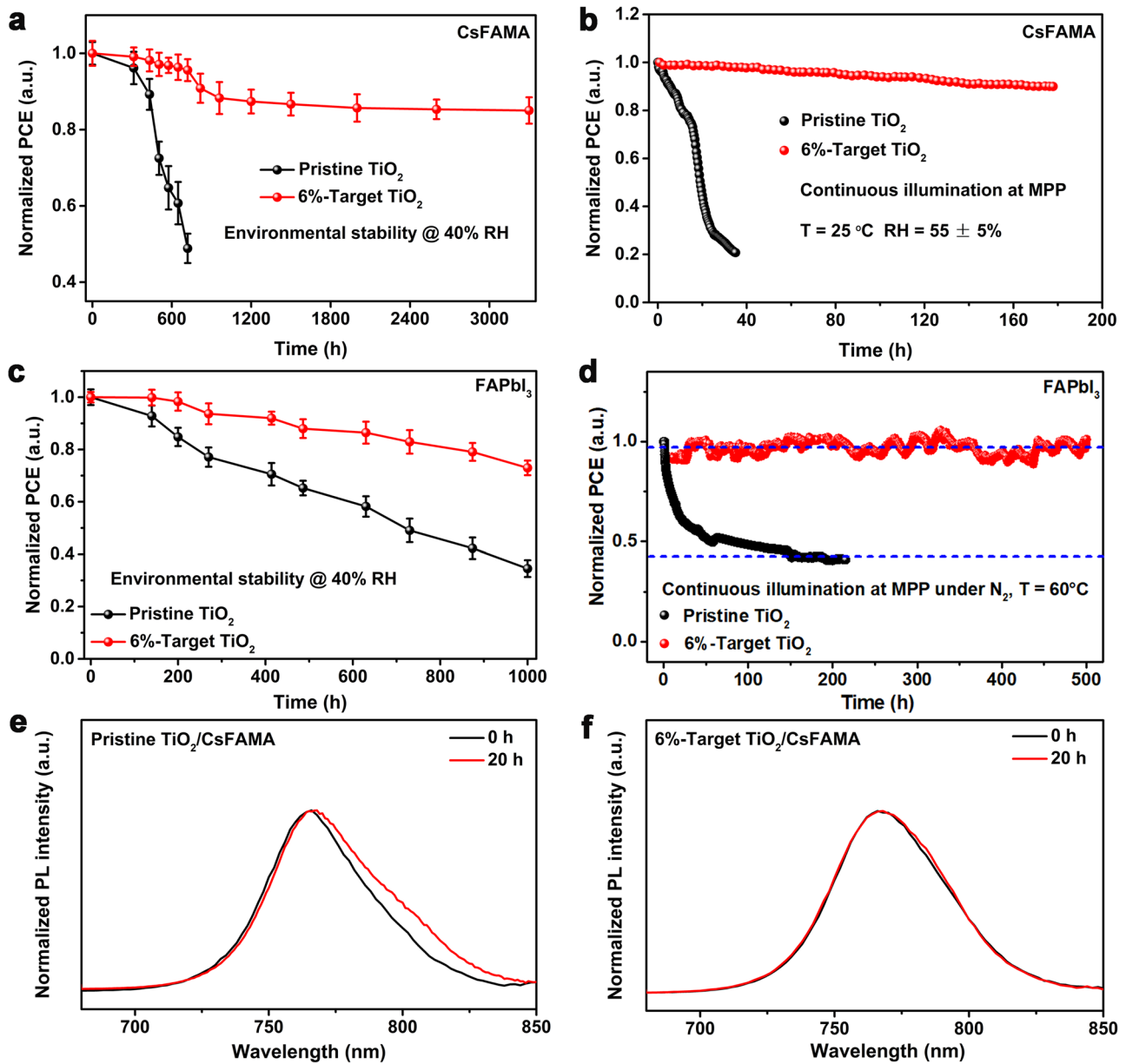


Fig. 4 **a** Humidity stability and **b** operational stability of different CsFAMA-based devices. **c** Humidity stability and **d** operational stability of different FAPbI₃-based devices. Normalized PL spectra of perovskite films grown on **e** pristine TiO₂ and **f** 6%-target TiO₂ layers under continuous 254 nm UV irradiation (50 mW cm⁻²) for 20 h. The error bars represent the standard deviation for 20 devices

TiO₂ could not only accelerate the electron transport at both the surfaces and the boundaries of TiO₂ matrix due to the increase in depletion width [19], but also significantly enhance crystal quality of the ETLs, resulting in enhanced conduction capability and boosted electron mobility by two orders of magnitude for TiO₂ ETLs; (ii) such p–n homo-junction enables upward-shifted Fermi level of TiO₂ that favors better energy level alignment with the perovskite,

leading thus to reduction in voltage loss and promotion of electron extraction at the buried interface [31]; (iii) embedding Ti_{0.936}O₂ could greatly improve not only crystallization process of TiO₂ for the inhibition of rutile phase that results in light-induced instability (Fig. S29), but surface wettability of TiO₂ that initiates rapid nucleation of top precursor for the fabrication of highly crystalline and large-grain perovskite films, which effectively prevent moisture from penetrating

at grain boundaries to retard degradation of perovskite and enhance humidity stability of PSCs. Owing to these merits, highly efficient FAPbI₃ PSCs delivered champion PCE up to 25.50%, which ranks among the top in records of TiO₂-based planar PSCs, as well as prominent moisture (RH of 40% for 3300 h) and light (under MPP for 500 h) stability of unencapsulated PSCs were achieved. It could be inferred from the improvement of all photovoltaic parameters that better energy level alignment, accelerated electron transport and reduced contact impedance at the buried interface principally account for the increment of V_{oc} , J_{sc} , and FF , respectively [11, 23, 24]. In addition, the significantly eliminated hysteresis phenomenon of the target device is attributed to effective suppression of the carrier transport imbalance within the device, due to the enhanced electron mobility of the ETLs by embedding Ti_{0.936}O₂ (Figs. 3b and S30, Tables S4 and S7) [32].

4 Conclusions

In summary, present work has demonstrated an efficient strategy of laser embedding of the p–n homojunctions in TiO₂ ETLs to address the issues of insufficient carrier transport at the buried interface for highly efficient and stable PSCs. The embedded p–n homojunction between Ti_{0.936}O₂ and TiO₂ not only greatly assisted synchronous acceleration of carrier transport at both surfaces and boundaries of TiO₂, which principally accounts for boosted electron mobility by two orders of magnitude, but modulates interfacial energy level to rapidly extract electrons that results in reduction of voltage deficit. The laser generated p-type Ti_{0.936}O₂ also exerts significant influence on the crystallization kinetics of the TiO₂ matrix and top precursor, which significantly inhibits the rutile phase that leads to light instability and initiates the fabrication of large-grain perovskite that enhances humidity stability of PSCs, respectively. The capability of such novel Ti_{0.936}O₂@TiO₂ ETLs is thus demonstrated by accessing efficient and stable planar FAPbI₃ PSCs with a champion efficiency of 25.50% and robust light-induced stability over 500 h, as well as mixed-cation PSCs with a champion efficiency of 22.02% and pronounced humidity stability for 3300 h (RH of 40%). This study exploits a novel pathway of developing highly conductive charge transport layers for state-of-the-art planar PSCs.

Acknowledgements This work was financially supported by the project of the National Natural Science Foundation of China (52202115 and 52172101), the China Postdoctoral Science Foundation (2022M722586), the Natural Science Foundation of Chongqing, China (CSTB2022NSCQ-MSX1085), the Shaanxi Science and Technology Innovation Team (2023-CX-TD-44), the Fundamental Research Funds for the Central Universities (3102019JC005 and G2022KY0604). The authors would like to thank the Analytical & Testing Center of Northwestern Polytechnical University and Shaanxi Materials Analysis and Research Center for XPS, XRD, SEM and TEM characterizations.

Author Contributions HW and PG have proposed the concept and directed the research. WZ, JW, DL and NJ performed the synthesis of materials and devices. ZF and CL carried out the characterization of materials and devices. WZ and PG finished writing the manuscript. QY, JZ, YZ put forward suggestions on the research. All the authors participated in the discussion of the results.

Declarations

Conflict of interest The authors declare that they have no conflict of interest. They have no known competing financial interests or personal relationships that could have appeared to influence the work reported in this paper.

Open Access This article is licensed under a Creative Commons Attribution 4.0 International License, which permits use, sharing, adaptation, distribution and reproduction in any medium or format, as long as you give appropriate credit to the original author(s) and the source, provide a link to the Creative Commons licence, and indicate if changes were made. The images or other third party material in this article are included in the article's Creative Commons licence, unless indicated otherwise in a credit line to the material. If material is not included in the article's Creative Commons licence and your intended use is not permitted by statutory regulation or exceeds the permitted use, you will need to obtain permission directly from the copyright holder. To view a copy of this licence, visit <http://creativecommons.org/licenses/by/4.0/>.

Supplementary Information The online version contains supplementary material available at <https://doi.org/10.1007/s40820-024-01407-3>.

References

1. J. Park, J. Kim, H.S. Yun, M.J. Paik, E. Noh et al., Controlled growth of perovskite layers with volatile alkylammonium chlorides. *Nature* **616**, 724–730 (2023). <https://doi.org/10.1038/s41586-023-05825-y>
2. S. Yu, Z. Xiong, H. Zhou, Q. Zhang, Z. Wang et al., Homogenized NiO_x nanoparticles for improved hole transport in inverted perovskite solar cells. *Science* **382**, 1399–1404 (2023). <https://doi.org/10.1126/science.adj8858>

3. Z. Liang, Y. Zhang, H. Xu, W. Chen, B. Liu et al., Homogenizing out-of-plane cation composition in perovskite solar cells. *Nature* **624**, 557–563 (2023). <https://doi.org/10.1038/s41586-023-06784-0>
4. X. Ji, L. Bi, Q. Fu, B. Li, J. Wang et al., Target therapy for buried interface enables stable perovskite solar cells with 25.05% efficiency. *Adv. Mater.* **35**, e2303665 (2023). <https://doi.org/10.1002/adma.202303665>
5. W. Zhao, P. Guo, C. Liu, N. Jia, Z. Fang et al., Laser derived electron transport layers with embedded p-n heterointerfaces enabling planar perovskite solar cells with efficiency over 25%. *Adv. Mater.* **35**, e2300403 (2023). <https://doi.org/10.1002/adma.202300403>
6. D. Yang, R. Yang, K. Wang, C. Wu, X. Zhu et al., High efficiency planar-type perovskite solar cells with negligible hysteresis using EDTA-complexed SnO₂. *Nat. Commun.* **9**, 3239 (2018). <https://doi.org/10.1038/s41467-018-05760-x>
7. J. Peng, F. Kremer, D. Walter, Y. Wu, Y. Ji et al., Centimetre-scale perovskite solar cells with fill factors of more than 86 per cent. *Nature* **601**, 573–578 (2022). <https://doi.org/10.1038/s41586-021-04216-5>
8. C. Luo, G. Zheng, F. Gao, X. Wang, C. Zhan et al., Engineering the buried interface in perovskite solar cells via lattice-matched electron transport layer. *Nat. Photonics* **17**, 856–864 (2023). <https://doi.org/10.1038/s41566-023-01247-4>
9. M.M. Byranvand, T. Kim, S. Song, G. Kang, S.U. Ryu et al., P-type CuI islands on TiO₂ electron transport layer for a highly efficient planar-perovskite solar cell with negligible hysteresis. *Adv. Energy Mater.* **8**, 1702235 (2018). <https://doi.org/10.1002/aenm.201702235>
10. P. Cui, D. Wei, J. Ji, H. Huang, E. Jia et al., Planar p–n homojunction perovskite solar cells with efficiency exceeding 21.3%. *Nat. Energy* **4**, 150–159 (2019). <https://doi.org/10.1038/s41560-018-0324-8>
11. P. Guo, H. Zhu, W. Zhao, C. Liu, L. Zhu et al., Interfacial embedding of laser-manufactured fluorinated gold clusters enabling stable perovskite solar cells with efficiency over 24. *Adv. Mater.* **33**, e2101590 (2021). <https://doi.org/10.1002/adma.202101590>
12. H. Li, R. Zhang, Y. Li, Y. Li, H. Liu et al., Graphdiyne-based bulk heterojunction for efficient and moisture-stable planar perovskite solar cells. *Adv. Energy Mater.* **8**, 1802012 (2018). <https://doi.org/10.1002/aenm.201802012>
13. S. Wang, L. Pan, J.-J. Song, W. Mi, J.-J. Zou et al., Titanium-defected undoped anatase TiO₂ with p-type conductivity, room-temperature ferromagnetism, and remarkable photocatalytic performance. *J. Am. Chem. Soc.* **137**, 2975–2983 (2015). <https://doi.org/10.1021/ja512047k>
14. F. Li, J. Jian, J. Zou, S. Wang, Z. Zhang et al., Bulk embedding of Ti-defected TiO₂ nano-heterointerfaces in hematite photoanode for boosted photoelectrochemical water splitting. *Chem. Eng. J.* **473**, 145254 (2023). <https://doi.org/10.1016/j.cej.2023.145254>
15. M. Gopal, W.J. Moberly Chan, L.C. De Jonghe, Room temperature synthesis of crystalline metal oxides. *J. Mater. Sci.* **32**, 6001–6008 (1997). <https://doi.org/10.1023/A1018671212890>
16. W. Hu, W. Zhou, X. Lei, P. Zhou, M. Zhang et al., Low-temperature *in situ* amino functionalization of TiO₂ nanoparticles sharpens electron management achieving over 21% efficient planar perovskite solar cells. *Adv. Mater.* **31**, 1806095 (2019). <https://doi.org/10.1002/adma.201806095>
17. X. Wang, S. Shen, Z. Feng, C. Li, Time-resolved photoluminescence of anatase/rutile TiO₂ phase junction revealing charge separation dynamics. *Chin. J. Catal.* **37**, 2059–2068 (2016). [https://doi.org/10.1016/s1872-2067\(16\)62574-3](https://doi.org/10.1016/s1872-2067(16)62574-3)
18. J. Zheng, Z. Lei, Incorporation of CoO nanoparticles in 3D marigold flower-like hierarchical architecture MnCo₂O₄ for highly boosting solar light photo-oxidation and reduction ability. *Appl. Catal. B Environ.* **237**, 1–8 (2018). <https://doi.org/10.1016/j.apcatb.2018.05.060>
19. S. Ye, H. Rao, Z. Zhao, L. Zhang, H. Bao et al., A breakthrough efficiency of 19.9% obtained in inverted perovskite solar cells by using an efficient trap state passivator Cu(thiourea)I. *J. Am. Chem. Soc.* **139**, 7504–7512 (2017). <https://doi.org/10.1021/jacs.7b01439>
20. M. Liu, Y. Chen, C.-S. Tan, R. Quintero-Bermudez, A.H. Proppe et al., Lattice anchoring stabilizes solution-processed semiconductors. *Nature* **570**, 96–101 (2019). <https://doi.org/10.1038/s41586-019-1239-7>
21. P. Guo, C. Liu, X. Li, Z. Chen, H. Zhu et al., Laser manufactured nano-MXenes with tailored halogen terminations enable interfacial ionic stabilization of high performance perovskite solar cells. *Adv. Energy Mater.* **12**, 2202395 (2022). <https://doi.org/10.1002/aenm.202202395>
22. D. Yang, X. Zhou, R. Yang, Z. Yang, W. Yu et al., Surface optimization to eliminate hysteresis for record efficiency planar perovskite solar cells. *Energy Environ. Sci.* **9**, 3071–3078 (2016). <https://doi.org/10.1039/C6EE02139E>
23. W. Zhao, P. Guo, J. Su, Z. Fang, N. Jia et al., Synchronous passivation of defects with low formation energies via terdentate anchoring enabling high performance perovskite solar cells with efficiency over 24%. *Adv. Funct. Mater.* **32**, 2200534 (2022). <https://doi.org/10.1002/adfm.202200534>
24. P. Guo, X. Yang, Q. Ye, J. Zhang, H. Wang et al., Laser-generated nanocrystals in perovskite: universal embedding of ligand-free and sub-10 nm nanocrystals in solution-processed metal halide perovskite films for effectively modulated optoelectronic performance. *Adv. Energy Mater.* **9**, 1901341 (2019). <https://doi.org/10.1002/aenm.201901341>
25. X. Gong, L. Guan, Q. Li, Y. Li, T. Zhang et al., Black phosphorus quantum dots in inorganic perovskite thin films for efficient photovoltaic application. *Sci. Adv.* **6**, eaay5661 (2020). <https://doi.org/10.1126/sciadv.aay5661>
26. J. Li, L. Xie, Z. Pu, C. Liu, M. Yang et al., The synergistic effect of pemirolost potassium on carrier management and strain release for high-performance inverted perovskite solar cells. *Adv. Funct. Mater.* **33**, 2301956 (2023). <https://doi.org/10.1002/adfm.202301956>



27. L. Xie, X. Zhao, J. Wang, J. Li, C. Liu et al., Multifunctional anchoring of O-ligands for high-performance and stable inverted perovskite solar cells. *InfoMat* **5**, e12379 (2023). <https://doi.org/10.1002/inf2.12379>
28. L. Xie, J. Liu, J. Li, C. Liu, Z. Pu et al., A deformable additive on defects passivation and phase segregation inhibition enables the efficiency of inverted perovskite solar cells over 24%. *Adv. Mater.* **35**, 2302752 (2023). <https://doi.org/10.1002/adma.202302752>
29. J. Jeong, M. Kim, J. Seo, H. Lu, P. Ahlawat et al., Pseudo-halide anion engineering for α -FAPbI₃ perovskite solar cells. *Nature* **592**, 381–385 (2021). <https://doi.org/10.1038/s41586-021-03406-5>
30. H. Huang, P. Cui, Y. Chen, L. Yan, X. Yue et al., 24.8%-efficient planar perovskite solar cells via ligand-engineered TiO₂ deposition. *Joule* **6**, 2186–2202 (2022). <https://doi.org/10.1016/j.joule.2022.07.004>
31. M.A. Rahman, Numerical modeling of ultra-thin CuSbS₂ heterojunction solar cell with TiO₂ electron transport and CuAlO₂: Mg BSF layers. *Opt. Mater. Express* **12**, 2954–2973 (2022). <https://doi.org/10.1364/OME.465498>
32. K. Chen, Q. Hu, T. Liu, L. Zhao, D. Luo et al., Charge-carrier balance for highly efficient inverted planar heterojunction perovskite solar cells. *Adv. Mater.* **28**, 10718–10724 (2016). <https://doi.org/10.1002/adma.201604048>